The Astrophysical Journal, 951:55 (16pp), 2023 July 1 https://doi.org/10.3847/1538-4357/acd10b

The Solar Minimum Eclipse of 2019 July 2. III. Inferring the Coronal T_e with a Radiative Differential Emission Measure Inversion

Benjamin Boe[1], Cooper Downs[2], and Shadia Habbal[1]
[1] Institute for Astronomy, University of Hawaii, Honolulu, HI 96822, USA; bboe@hawaii.edu
[2] Predictive Science Inc., San Diego, CA 92121, USA

Received 2023 February 21; revised 2023 April 6; accepted 2023 April 17; published 2023 July 3

Abstract

Differential emission measure (DEM) inversion methods use the brightness of a set of emission lines to infer the line-of-sight (LOS) distribution of the electron temperature (T_e) in the corona. DEM inversions have been traditionally performed with collisionally excited lines at wavelengths in the extreme ultraviolet and X-ray. However, such emission is difficult to observe beyond the inner corona (1.5 $R_\odot$), particularly in coronal holes. Given the importance of the T_e distribution in the corona for exploring the viability of different heating processes, we introduce an analog of the DEM specifically for radiatively excited coronal emission lines, such as those observed during total solar eclipses (TSEs) and with coronagraphs. This radiative-DEM (R-DEM) inversion utilizes visible and infrared emission lines that are excited by photospheric radiation out to at least 3 $R_\odot$. Specifically, we use the Fe X (637 nm), Fe XI (789 nm), and Fe XIV (530 nm) coronal emission lines observed during the 2019 July 2 TSE near solar minimum. We find that, despite a large T_e spread in the inner corona, the distribution converges to an almost isothermal yet bimodal distribution beyond 1.4 $R_\odot$, with T_e ranging from 1.1 to 1.4 in coronal holes and from 1.4 to 1.65 MK in quiescent streamers. Application of the R-DEM inversion to the Predictive Science Inc. magnetohydrodynamic simulation for the 2019 eclipse validates the R-DEM method and yields a similar LOS T_e distribution to the eclipse data.

Unified Astronomy Thesaurus concepts: Solar corona (1483); Solar eclipses (1489); Solar coronal streamers (1486); Solar coronal holes (1484); Solar optical telescopes (1514)

Supporting material: animation

1. Introduction

Differential emission measure (DEM) inversion techniques combine observations of multiple emission lines to infer the line-of-sight (LOS) distribution of the electron temperature (T_e) in an optically thin plasma, such as the solar corona. DEM inversions are commonly used to explore coronal thermodynamics with emission lines at X-ray (e.g., Pottasch 1964; Kepa et al. 2006, 2022) and extreme ultraviolet (EUV; e.g., Withbroe 1978; Cheng et al. 2012; Hannah & Kontar 2012; Cheung et al. 2015) wavelengths. EUV DEMs are a useful tool for inferring T_e in active regions (Aschwanden et al. 2015) and the solar cycle dependence of T_e in the corona (Morgan & Taroyan 2017). X-ray DEMs have even been used to study the temperature of stellar coronae (Güdel et al. 2001).

A significant limitation of DEM inversion analysis based on X-ray and EUV lines is that the lines are predominantly collisionally excited, which means the emission is proportional to the density squared, and so they decline in brightness rapidly at larger helioprojective distances. There can be radiative excitation of EUV lines but that requires flux from the same collisionally excited line lower down in the corona (the solar disk does not emit any meaningful amount of EUV photons). Recent developments have proven that EUV lines can be detected out to 2 $R_\odot$ with Proba-2/SWAP (Goryaev et al. 2014) and 2.5 $R_\odot$ with GOES/SUVI (Seaton et al. 2021), but the EUV lines are difficult to observe beyond 1.5 $R_\odot$, and the relative contribution of resonant scattering is not as well characterized since its source brightness (i.e., emission from the low corona) has spatial and temporal variation. The visible and infrared coronal lines, on the other hand, can be radiatively excited by photospheric emission and, in turn, can often be observed at helioprojective distances of up to 3.4 $R_\odot$ or more (see Boe et al. 2022).

Another drawback of DEM inversion performed specifically with bandpasses in the EUV is that multiple lines are present in each bandpass and so the observed brightness leads to complex temperature response functions (e.g., O'Dwyer et al. 2010; Boerner et al. 2012). Solving a DEM with EUV observations is therefore rather challenging; it requires nontrivial inversion methods (e.g., Guennou et al. 2012a, 2012b; Hannah & Kontar 2012; Aschwanden et al. 2015; Morgan & Pickering 2019) and clever techniques to reduce the computationally expensive operation (e.g., Kashyap & Drake 1998; Plowman et al. 2013; Cheung et al. 2015; Pickering & Morgan 2019). (See Del Zanna & Mason 2018 for a detailed overview of the history of DEM inversion methods and applications)

Outside of EUV and X-ray DEM inversions, the coronal electron temperature has been inferred with emission-line ratios at wavelengths in the ultraviolet from space (e.g., Raymond et al. 1997; Ko et al. 2002) and in the visible and infrared during total solar eclipses (e.g., Boe et al. 2020a, 2022; Del Zanna et al. 2023). Without emission lines, the effective temperature has been inferred using the density profile inferred from polarized brightness measurements (e.g., Munro & Jackson 1977). However, the effective temperature is a combination of the electron and proton temperatures, which will follow significantly different profiles (see Esser et al. 1997). Isolating the electron and proton temperatures using continuum-based analysis is thus not possible without other data or assumptions (e.g., Doyle et al. 1999). The electron temperature of the corona can also be deduced from in situ measurements of ionic composition (e.g., Ko et al. 1996, 1997; Smith et al. 2003; Habbal et al. 2010; Landi & Testa 2014) since the ions will cease charge-exchange processes at some distance from the Sun (i.e., they freeze-in their ionic state; see Boe et al. 2018; Gilly & Cranmer 2020). Unfortunately, any in situ driven analysis lacks precise information about the coronal structure (and freeze-in distance) from which each solar wind parcel originated. None of these methods have provided a complete survey of the distribution of the electron temperature throughout the corona and in all but a few cases are only able to probe very small portions of the corona. Only visible and infrared emission-line observations have shown the potential to quantify the LOS T_e distribution throughout the entire middle corona from below 1.5 $R_\odot$ to perhaps as much as 6 $R_\odot$.

In this paper, we implement a new radiative-DEM (R-DEM) method, which is introduced for lines that are radiatively excited (see Section 3). The R-DEM is applied to observations of the Fe X (637.5 nm), Fe XI (789.2 nm), and Fe XIV (530.3 nm) emission lines from the 2019 total solar eclipse (TSE; see Section 2). We also implement the R-DEM method on forward-modeled line emission from the Predictive Science Inc. (PSI) magnetohydrodynamic (MHD) simulation (see Section 4.2) and compare the inversion results to the actual T_e distribution along the LOS in the MHD model. We discuss the details of the findings, including comparisons between the eclipse and model inferences and actual LOS T_e distribution in Section 5. Concluding remarks are given in Section 6.

2. 2019 July 2 Total Solar Eclipse

To explore the T_e distribution in the corona with a new R-DEM inversion procedure (see Section 3), we use visible observations of the brightness of Fe X (637.5 nm), Fe XI (789.2 nm), and Fe XIV (530.3 nm), which were acquired during the 2019 July 2 TSE in Rodeo, Argentina. This eclipse occurred very close to solar minimum when the corona was dominated by a dipolar field component, as showcased by the white-light eclipse image and the magnetic field line extrapolation of the PSI MHD model (see Section 4.2) in the top panels of Figure 1. The brightness of the emission lines was acquired with narrowband telescope systems that have been deployed at a number of recent TSEs (see Boe et al. 2018, 2020a; Habbal et al. 2021).

The temperature responses of the Fe X, Fe XI, and Fe XIV lines span coronal electron temperatures (T_e) from 0.8 to 2.5 MK. The ionic equilibrium curves that we use in this work are shown in the top panel of Figure 2. The curves are generated from version 10 of the CHIANTI database (Dere et al. 1997; Del Zanna et al. 2021), which have been interpolated from their recorded spacing of $\Delta\log(\mathrm{K}) = 0.05$. Higher-$T_e$ plasma can exist in active regions below 1.2 $R_\odot$, but the vast majority of coronal plasmas that escape into the solar wind are found to have a coronal temperature between 1 and 2 MK (Habbal et al. 2021). Further, this eclipse occurred near solar minimum when there were no active regions on the Sun.

To isolate the line emission, we use one telescope with a bandpass centered on the wavelength of the emission line and another about 1–3 nm away from the line to observe the background continuum brightness. The set of continuum observations from this eclipse was used by Boe et al. (2021) (Paper I) to study the K (electron) and F corona (dust) brightness using a novel color-based inference method. The calibration for the continuum data was leveraged off the Mauna Loa Solar Observatory's (MLSO) K-coronagraph (K-Cor)[3] polarized brightness data from the same day as the eclipse. The inferred K corona brightness from Paper I can be found in the middle-left panel of Figure 1. Boe et al. (2022) (Paper II) then extended the calibration to the simultaneous line-emission observations to isolate the brightness of Fe X, Fe XI, and Fe XIV.

In Paper II, we inferred the LOS-integrated ionic column density ratio, which we will use in this work to perform the R-DEM inversion. Specifically, we isolated the radiative component of the line-emission observations by removing the fraction of brightness that originated from collisional excitation based on the PSI MHD model (see Section 4.2). The radiative line ratios were then used to infer the integrated column density ratios of Fe X/Fe XI and Fe XIV/Fe XI after accounting for the atomic radiation processes of each ion as well as the effect of variable line widths integrated over each bandpass at different helioprojective distances (based on previous observations). Note that since these ratios are integrated along the same LOS, they are equivalent both to the column density ratio as well as the average volumetric density ratio along each LOS.

The final inferred ionic density ratios are shown in the bottom-middle panels of Figure 1. These ionic density ratio maps clearly show that Fe XI is the most abundant ion of the three. Fe X has a similar density in the low corona (below 1.3 $R_\odot$) but declines relative to Fe XI at higher helioprojective distances. As for the Fe XIV ion, it has a similar density to Fe XI in the cores of the coronal streamers but is otherwise significantly less abundant than Fe XI. Paper II then took these ionic equilibrium density ratios and inferred T_e in the corona, using the correspondence between the ionic equilibrium and T_e (i.e., the curves shown in the bottom panel of Figure 2). The Fe XI/Fe X ratio in particular did not return a realistic average T_e, likely due to the very shallow slope of the density ratio versus T_e curve. The other two T_e inferences, from the Fe XIV/Fe X and Fe XIV/Fe XI ionic density ratios, are shown in the bottom-right panels of Figure 2. In this work, we implement a new R-DEM procedure that uses the corrected Fe X/Fe XI and Fe XIV/Fe XI inferred density ratios to infer the LOS distribution of T_e in the corona.

3. Radiative Differential Emission Measure

3.1. R-DEM Formalism

The traditional DEM is defined as (see Withbroe 1978; Del Zanna & Mason 2018)

$$\mathrm{DEM}(T_e) = N_e^2 \frac{dh}{dT_e}, \qquad (1)$$

where N_e is the electron density (squared since it is causing collisional excitation of the ions). The DEM represents the density-squared-weighted T_e distribution along a given LOS, in units of cm^{-5} K^{-1}.

The brightness, β_i, of an emission line i from an ion of element Z with elemental abundance $Ab(Z)$ can be related to the integral of the temperature over the contribution function, $C_i(T_e, N_e, \lambda_i)$, multiplied by the DEM function. The brightness

---

[3] https://mlso.hao.ucar.edu/mlso_data_calendar.php

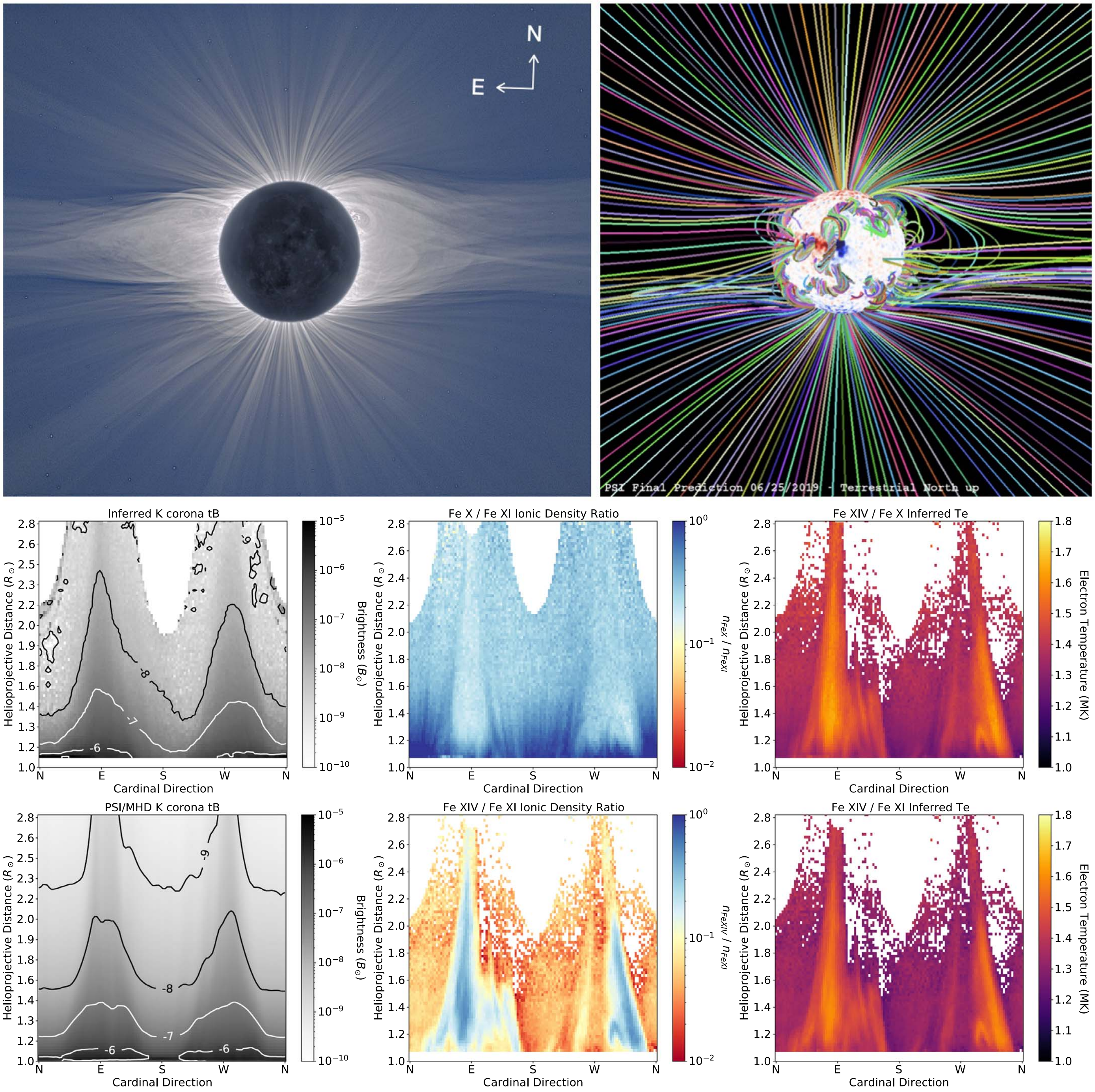

Figure 1. Top left: white-light image of the 2019 TSE (first presented in Boe et al. 2020b). Top right: PSI MHD model field-line prediction of the eclipse (see Section 4.2). The bottom two rows contain a collection of inferred (and modeled) coronal properties in a Cartesian representation of polar coordinates from Boe et al. (2021, 2022). Bottom left: K corona brightness from the eclipse (middle) and PSI MHD model (bottom). Bottom middle: inferred ionic density ratio of Fe X/Fe XI (middle) and Fe XIV/Fe XI (bottom). Bottom right: inferred T_e from the Fe XIV/Fe X (middle) and Fe XIV/Fe XI (bottom) ionic density ratios.

is then

$$\beta_i = Ab(Z) \int_{T_e} C_i(T_e, N_e, \lambda_i)\, \mathrm{DEM}(T_e)\, dT_e. \tag{2}$$

The traditional DEM formulation only works for collisionally excited lines, which are the main type of line emission one can usually expect at X-ray and EUV wavelengths (see Section 1). The contribution function is thus a complicated interdependence of the nature of the given ionic line transition, the electron density (since the lines are collisionally exited), and the temperature dependence of the ionic species.

For the visible lines observed during the eclipse, on the other hand, the lines are almost entirely radiatively excited and so a different formalism is required. We thus introduce a slightly modified R-DEM, which will replace the DEM(T_e) term in Equation (2), where

$$\mathrm{RDEM}(T) = N_e \frac{dh}{dT}, \tag{3}$$

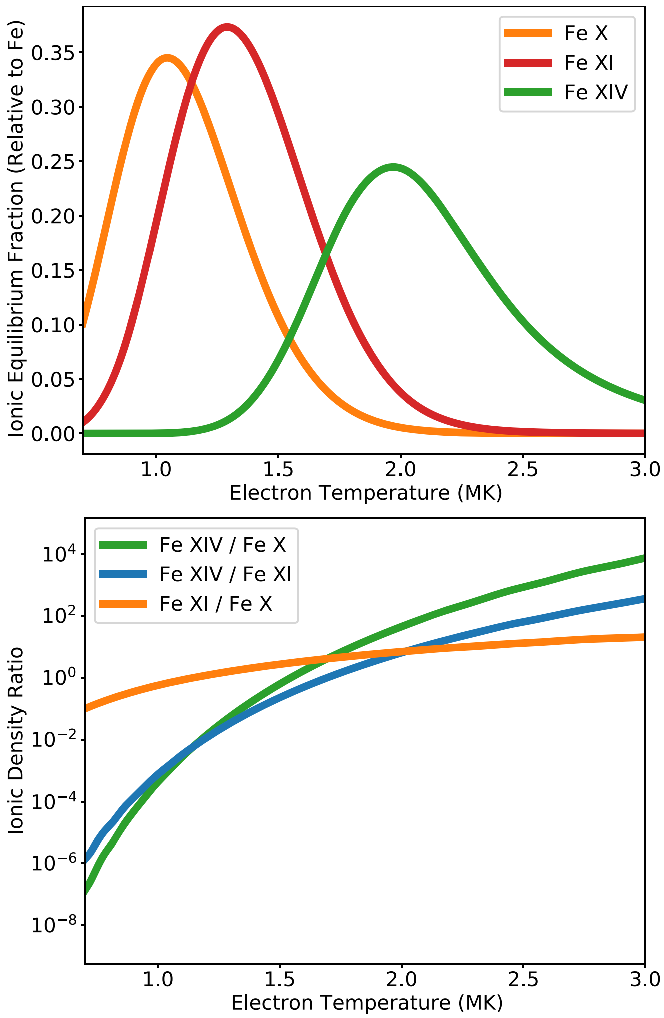

Figure 2. Top: ionic equilibrium curves of Fe X, Fe XI, and Fe XIV vs. T_e with values interpolated from CHIANTI. Bottom: ionic equilibrium density ratios vs. T_e from the curve above.

which will have units of $\mathrm{cm}^{-2}\ \mathrm{K}^{-1}$. Unlike the collisional DEM inversion, the R-DEM inversion has a significantly simpler contribution function as it does not depend on the electron density (i.e., $C_i(T_e,\ \lambda_i)$). Rather, it is only a combination of the straightforward radiative ionic transition parameters based on radiative excitation from the photospheric emission combined with the temperature response of the ion (i.e., the curves in the top panel of Figure 2). The brightness of a radiatively excited line is then

$$\beta_i = Ab(Z) \int_{T_e} C_i(T_e,\ \lambda_i)\ \mathrm{RDEM}(T_e)\ dT_e. \tag{4}$$

One can also calculate the radiative emission measure, or R-EM, as the integral of the R-DEM over a defined temperature range of ΔT centered on temperature T_0,

$$\mathrm{REM}(T) = \int_{T_0-\frac{\Delta T}{2}}^{T_0+\frac{\Delta T}{2}} \mathrm{RDEM}(T)\ dT, \tag{5}$$

which represents the amount of emitting plasma at the specified temperature range in units of square centimeters.

Next, we simplify the inversion procedure given the particular properties of radiative excitation by using calibrated ionic column density ratios rather than the absolute emissivity. In Paper II, we used the ratio of the brightness between two radiative lines to infer the relative ionic density with the following equation:

$$\frac{n_j}{n_k} = \frac{\beta_j\ A_k\ g_{l,j}\ g_{u,k}\ {\nu_k}^3}{\beta_k\ A_j\ g_{u,j}\ g_{l,k}\ {\nu_j}^3}, \tag{6}$$

where for ions j and k, n is the number density, ν is the frequency of the line emission, A is the Einstein coefficient for spontaneous emission, and g is the statistical weight for the given energy level. Equation (6) assumes that the observed brightness β has been calibrated in solar disk units (i.e., $B_\odot$), thus removing the spectral dependency on the photospheric spectrum (see Boe et al. 2020a, 2022). It also assumes the brightness to be caused entirely by radiative excitation. The ionic density ratios as computed in Paper II already removed the collisional excitation component from the brightness using the ratio of the collisional and radiative excitation predicted by the PSI MHD simulation (which is only important in the streamers below $\approx$1.5 $R_\odot$). The calibrated ionic density ratios inferred in Paper II using Equation (6) for Fe X/Fe XI and Fe XIV/Fe XI are shown in the bottom-middle panels of Figure 1.

To express the R-DEM inversion in terms of the ionic density ratio, we take the ratio of the R-DEM brightness definition from Equation (4) and combine it with Equation (6), giving

$$\begin{aligned}\frac{\beta_j}{\beta_k} &= \frac{n_j\ A_j\ g_{u,j}\ g_{l,k}\ {\nu_j}^3}{n_k\ A_k\ g_{l,j}\ g_{u,k}\ {\nu_k}^3} \\ &= \frac{Ab(Z_j) \int C_j(T_e,\ \lambda_j)\ \mathrm{RDEM}(T_e)\ dT_e}{Ab(Z_i) \int C_k T_e,\ \lambda_k)\ \mathrm{RDEM}(T_e)\ dT_e},\end{aligned} \tag{7}$$

which reduces to

$$\frac{n_j}{n_k} = \frac{Ab(Z_j) \int {C'}_j(T_e)\ \mathrm{RDEM}(T_e)\ dT_e}{Ab(Z_k) \int {C'}_k(T_e)\ \mathrm{RDEM}(T_e)\ dT_e}. \tag{8}$$

The new contribution function, $C'(T_e)$, has now been simplified to remove all dependence on the line formation itself and instead is solely the temperature dependence of the ionic equilibrium (i.e., the curves in the top panel of Figure 2). The contribution function can be simplified in this way since the ionic density ratio has already accounted for the incident radiation and resonant excitation physics—a process that cannot be applied with traditional DEMs given the dependence of collisional excitation on density.

3.2. R-DEM Inversion Procedure

In this work, we will infer the R-DEM with the Fe X, Fe XI, and Fe XIV line observations. We thus apply Equation (8) to both the Fe XIV/Fe XI and Fe X/Fe XI ionic density ratios and fit a density distribution of the $\mathrm{RDEM}(T_e)$ that satisfies both ratios simultaneously (note that the elemental abundance terms disappear since we are only using Fe lines). That is, we use Fe XI as the reference density, scale the other densities by the inferred ionic density ratio, then solve for what R-DEM would best fit the two ratios of the integrals (i.e., Equation (8)).

Specifically, we use 201 bins of temperature ranging from 0.6 to 2.6 MK, with a spacing of 0.01 MK, and use the standard Python scipy `optimize.minimize`[4] function to fit the distribution of density coefficients. This optimization tool implements a Broyden–Fletcher–Goldfarb–Shanno algorithm, which is an iterative quasi-Newton method (default for `minimize`). The optimization procedure stops when it reaches the relative minimum of the difference between the inferred R-DEM and the observed ionic density ratios.

We initialized the temperature distribution as a uniform temperature distribution across the entire range from 0.6 to 2.6 MK. The function then varies the coefficients of each R-DEM bin to attempt to fit Equation (8) for both the Fe XIV/Fe XI and Fe X/Fe XI ionic density ratios simultaneously. Typically, the procedure terminated after about 100 iterations, with a maximum number of iterations at 310 for the eclipse data and 445 for the MHD modeled lines (we set the maximum number of iterations to 2000 to prevent premature termination). The resulting distribution provides the R-DEM for each LOS. A simple fit is sufficient for this R-DEM inversion since the temperature response functionality of the bandpasses shown in the top panel of Figure 2 is simple. Consequently, the combination of bandpass integrals quickly converges on a solution—even if only using these two ionic density ratios.

As with all optically thin plasmas, this inversion determines the integral over all structures along the LOS, which may well have different temperature distributions. The final inverted R-DEM should be thought of as the density-weighted temperature distribution along the entire LOS rather than for a well-defined volume of plasma.

In this inversion, we are not taking into account any geometric LOS or limb-darkening effects on the radiative excitation of the lines. Along each LOS, the emission lines will experience similar dynamics from changes in the size and apparent horizon of the extended solar disk. Thus, most of these effects are removed by considering the ratio of the lines independently for each LOS, unless there is a dramatic asymmetry in the distribution of plasma temperatures along the LOS. There will be slight differences in the limb-darkening profile at different wavelengths, but these changes should only lead to small differences in the final line emission. As described in Papers I and II, we did account for limb darkening when calibrating the absolute brightness of the lines, so we have already removed the limb-darkening effects somewhat. Finally, any effects of this kind will be most pronounced in the lowest part of the corona, which is also where we have to make corrections for collisional excitation using the MHD model. Clearly, the lower corona (below $\approx 1.3\ R_\odot$) is not as robustly probed by this particular R-DEM inversion compared to the outer corona. Since EUV DEMs already probe the lower corona regularly, the primary focus of this R-DEM inversion method is to infer the temperature distribution farther out in the corona, which is otherwise exceptionally difficult to measure.

4. Results

4.1. Eclipse R-DEM

A collection of RDEM(T_e) inferences for the observed emission lines (see Section 2) is shown in the top panels of Figures 3 and 4 for samples from the poles and equator, respectively. Each panel contains multiple sets of R-DEMs at different helioprojective distances ranging from 1.2 to 2.2 $R_\odot$, in steps of 0.2 $R_\odot$, inside of an 8° by 0.18 $R_\odot$ window centered on the various latitudinal regions. The R-DEM curves are colored according to the distance range they were taken at, as shown in the legend. Every individual R-DEM inversion result inside each distance range and latitudinal direction is shown as faint lines, while the median average of all R-DEMs in the window is shown as bold lines in the figure.

Each R-DEM is normalized by the integral of the R-DEM over all T_e bins to show the relative R-DEM distribution along the LOS rather than the density of the corona. The coronal density drops rapidly with distance, so for visualization, it makes more sense to present the results in this manner. These R-DEMs could be scaled by an inferred electron density of each region given a coronal density inversion using the polarized or total brightness of the K corona (a K corona map is shown in Figure 1). However, we are not concerned with the absolute density of the corona here; rather, we are interested in the relative T_e distribution throughout the corona.

To create a representative map of the R-DEM distributions, we took the weighted mean of the R-DEM from each LOS to infer an average T_e and the standard deviation (i.e., width) of the RDEM(T_e) distribution around the mean. The resulting maps are shown in the left panels of Figure 5. We then show a series of radial traces of the R-DEM at different latitudes in Figure 6 and latitudinal traces at a series of radial distances in Figure 7.

We find that the electron temperature generally varies from about 1.1 to 1.4 MK in the coronal holes, while the streamers are closer to 1.4–1.65 MK. The overall T_e values in the coronal holes rise considerably from around 1.1 MK at 1.1 $R_\odot$, up to almost 1.4 MK by about 1.4 $R_\odot$. The streamers have a similar behavior, where they also rise in T_e up to about 1.4 $R_\odot$. On the POS, the streamers have considerable spatial variation, with multiple distinguishable stalks, whereas the coronal holes have much less spatial variation. Below 1.4 $R_\odot$, there are a number of small cool plumes that extend into what appear to be closed field lines at the base of both the streamers and coronal holes.

The cores of the streamer have the highest T_e, especially in the eastern streamer, with values up to 1.65 MK. The western streamer is cooler in general, other than a closed loop and smaller stalk on the northwest side. The western streamer has a gap in the middle where the temperature is almost indistinguishable from the coronal holes, despite this region having higher electron densities (i.e., see the white-light image and K corona map in Figure 1). The width of the streamers also decreases considerably with height, occupying more than half of the corona at 1.2 $R_\odot$ but becoming only a very small portion by 2.6 $R_\odot$.

The width of the R-DEMs along each LOS indicates a large spread in the T_e throughout the corona (roughly ±0.1–0.3 MK) below about 1.4 $R_\odot$. However, beyond that distance, both the coronal holes and streamers appear almost entirely isothermal along the LOS with R-DEM widths less than ±0.05 MK (see Section 5.2).

4.2. PSI MHD R-DEM

Next, we test the effectiveness of the R-DEM procedure with the state-of-the-art MHD simulation of the PSI/MAS model prediction (Mikić et al. 2018) of this eclipse. Papers I and II used this MHD simulation to forward model the K corona and

---

[4] https://docs.scipy.org/doc/scipy/reference/generated/scipy.optimize.minimize.html#scipy.optimize.minimize

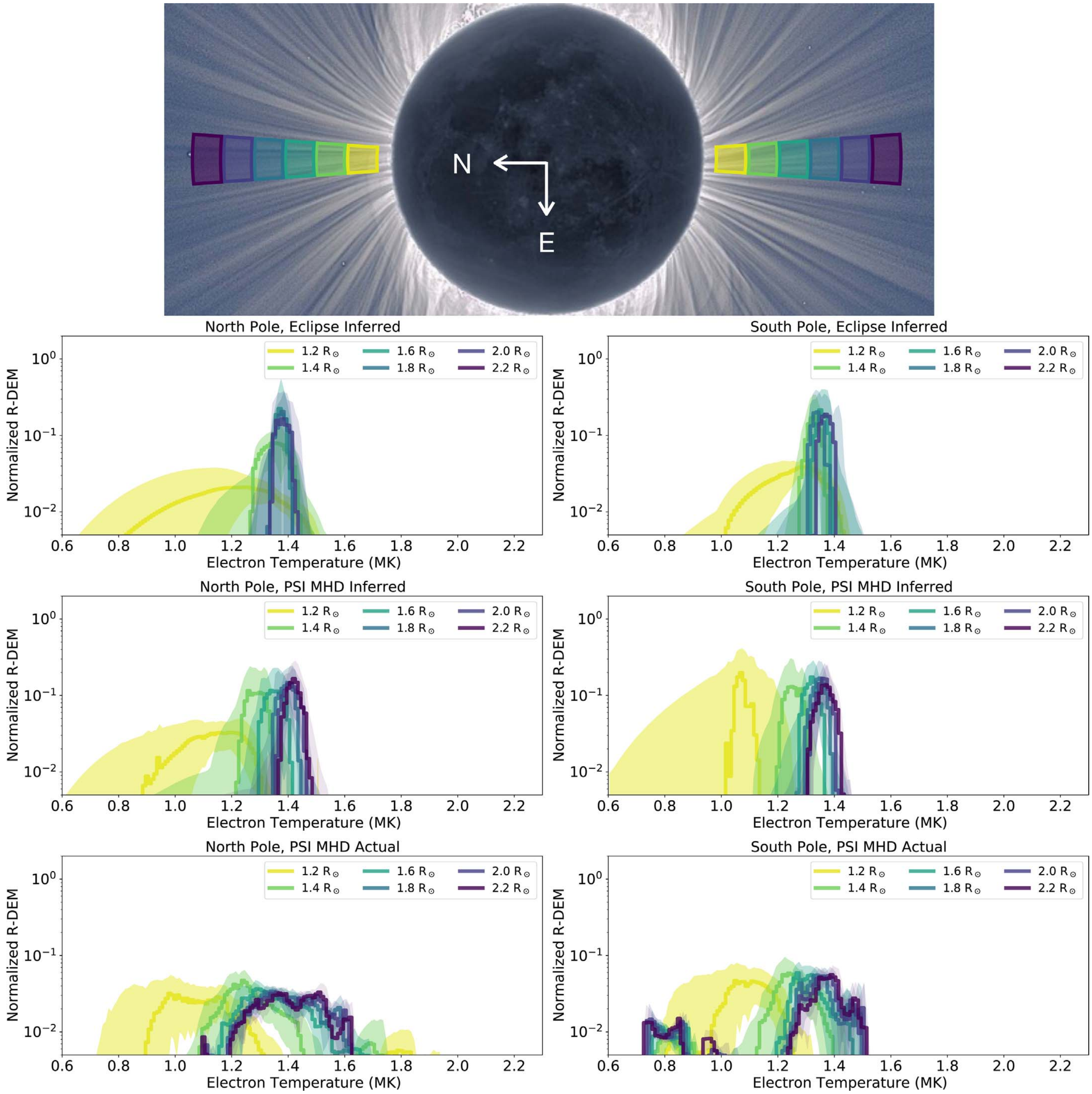

Figure 3. Collection of R-DEMs for the coronal holes at the poles of the Sun. The top panel contains the white-light image of the corona with a set of windows identified (8° by 0.18 $R_\odot$, steps of 0.2 $R_\odot$). The bottom panels show the R-DEM results for the north pole (left) and south pole (right), where the top panels are from the eclipse data (see Section 4.1), the middle panels are from the MHD forward-modeled lines (see Section 4.2), while the bottom panels are the actual R-DEMs in the MHD model (see Section 4.2.1). Every R-DEM inside each window is shown as a bold line, while the variance of the R-DEM distributions inside the window is shown as the shaded bands around each R-DEM curve.

line emission, respectively, and in both cases, the model was found to rather accurately predict the eclipse observations. The forward-modeled line emission can now be used to test the validity of the R-DEM approach by comparing the R-DEM inferred from the forward-modeled lines to the true LOS T_e distribution directly from the model. Using the same procedure described in Section 3.1, examples of the R-DEM inversion results are shown in Figures 3–7. In the same figures, we include the actual R-DEM from the MHD model in order to test the inversion process. In the Appendix, we further discuss the details of the R-DEM distribution inside the PSI MHD model.

The inferred T_e distribution from the MHD model is very similar to the eclipse R-DEM in general, although the model-inferred R-DEM has somewhat more variation in T_e throughout the POS and along the LOS. The eastern streamer in particular has a large T_e variance on the southern edge, which persists beyond at least 2.8 $R_\odot$.

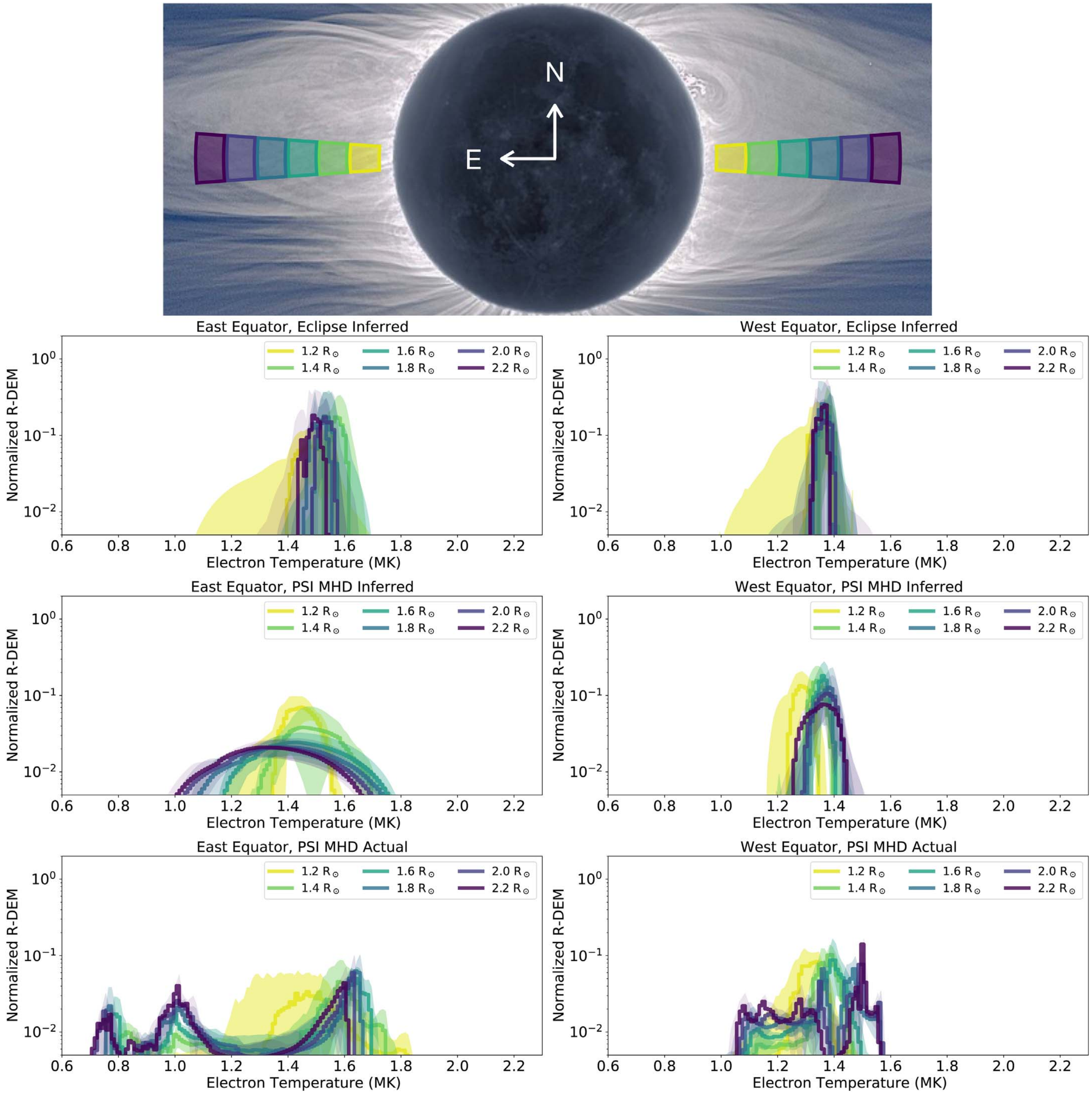

Figure 4. Same as Figure 3, except for windows centered on the streamers at the east (left) and west (right) equator. The white-light image has the same orientation as Figure 1.

4.2.1. Testing the R-DEM Inversion

To test the new R-DEM methodology, we compare the results from the actual LOS T_e distribution in the PSI MHD model with the inversion results from the forward-modeled lines. The actual R-DEMs, showcased in Figures 3–7, are quite similar to the inversion results, though the actual R-DEM shows a substantially wider T_e distribution with more fine-scale structures (see the Appendix). Still, the average T_e value is rather well recovered by the R-DEM inversion. A direct comparison between the average T_e in the actual versus inferred model results is shown in the top-left panel of Figure 8, where the inversion result is $4.6\% \pm 7.2\%$ higher than the actual R-DEM distribution. Further, while the inversion tends to underestimate the width of the R-DEM distribution, it is able to recover realistic R-DEM widths when the actual R-DEM is wider than about ±0.2 MK. Along the southeast streamer edge, for example, the R-DEM inversion correctly finds widths between ±0.3 and 0.4 MK.

It is not surprising that the inversion is unable to resolve the fine-scale T_e structures and smaller R-DEM widths since it only used three emission lines that have a somewhat broad temperature response compared to the shape of the actual

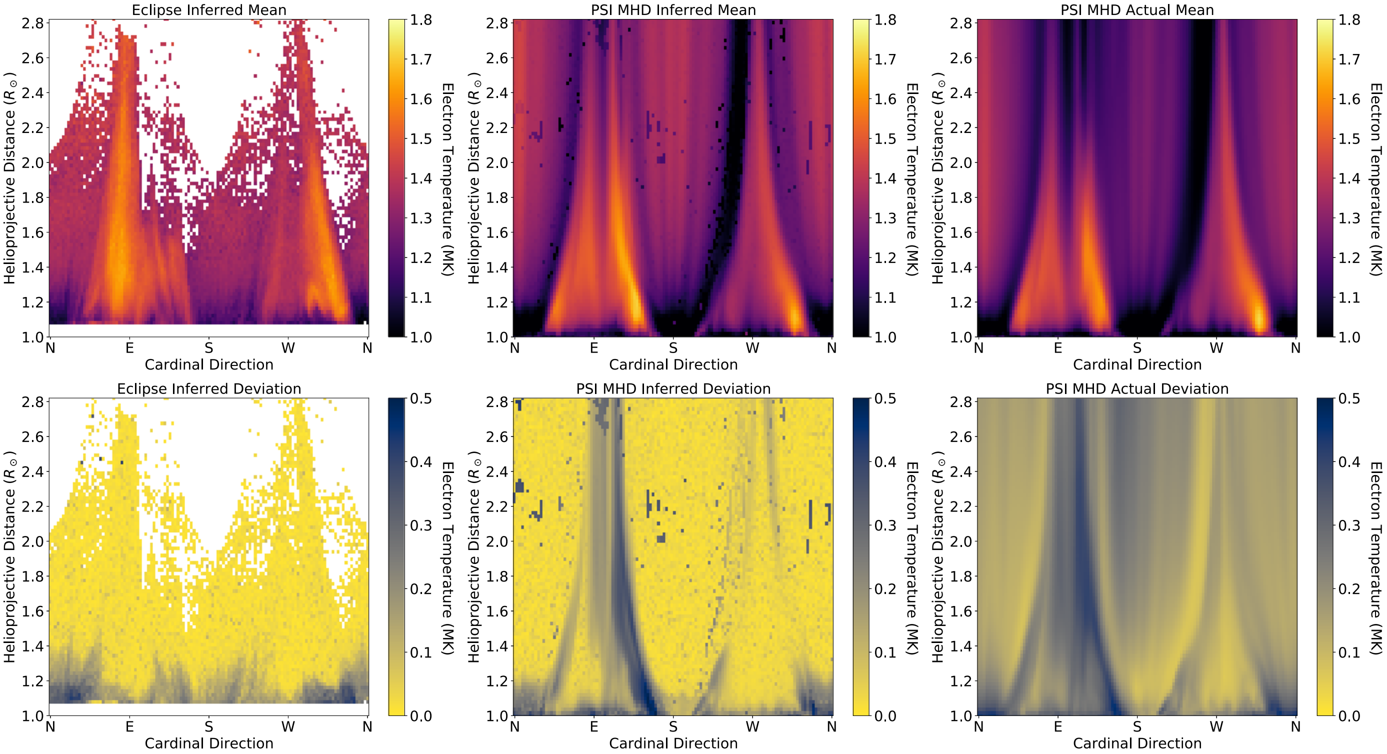

Figure 5. Top left: mean T_e from the R-DEM inversion from the eclipse lines. Bottom left: standard deviation of the R-DEM around the mean T_e. Middle: same as the left, for the MHD forward-modeled R-DEM inversion. Right: same as the left, for the actual R-DEM distribution in the MHD model.

R-DEM distribution, which reduces the precision that is possible to achieve. This effect is similar to the isothermal bias caused by two-line ratios (Weber et al. 2005) and, for some DEMs, depends on the temperature response curves of the instrument (Guennou et al. 2012a, 2012b). Future observations of additional lines such as Fe XIII (1074.7 nm) would increase the temperature resolution of a similar R-DEM inversion. Thus, any inferred R-DEM widths below about 0.2 MK are not necessarily accurate in the inversions presented here. Instead, smaller widths should be considered as below that sensitivity limit.

5. Discussion

In Section 3.1, we introduced the radiative analog of a DEM, called an R-DEM. We then applied this method in Section 4.1 to the Fe X, Fe XI, and Fe XIV data from the 2019 TSE (see Section 2), as well as to the forward-modeled emission lines from the PSI MHD prediction for this eclipse in Section 4.2. We compared the inferred model R-DEM distribution to the actual distribution of the MHD model in Section 4.2.1 to verify the accuracy of the inversion procedure. Now, we will discuss the R-DEM inversion results from both the eclipse and model and compare them to the actual LOS T_e distribution in the model.

5.1. *The* $\mathrm{T_e}$ *of Coronal Holes and Streamers*

The novelty of this work is not the finding of any particularly unexpected T_e values but rather that we have inferred the T_e values at a higher spatial resolution than has ever been achieved beyond the low corona (below 1.5 $R_\odot$) and that we have inferred the LOS variance of T_e (discussed in Section 5.2). EUV-based observations cannot constrain the electron temperature as far out as we have here, particularly in coronal holes where the signal is especially low. This high spatial resolution of the inference allows unique findings about both coronal holes and streamers.

We find the coronal holes to have electron temperatures of about 1.1–1.4 MK, where the values begin low, rise with helioprojective distance, then plateau at 1.4 MK by around 1.4 $R_\odot$. These values are somewhat higher than the estimate of 1.0–1.3 MK (for the same helioprojective distances) by Habbal et al. (1993), who reviewed a large number of earlier coronal hole T_e inferences using X-ray, EUV, and white-light data. These lower coronal hole T_e values are also consistent with many years of in situ charge state data of coronal holes (Smith et al. 2003; Habbal et al. 2010). One reason for this slight difference may not be due to actual differences in the electron temperature but rather due to changes in the ionic equilibrium estimates used to infer T_e. For example, the Fe ions used in this work had their equilibrium curves shifted to a higher temperature by approximately 0.1–0.15 MK in the more recent estimates in CHIANTI compared to older, commonly used computations such as Arnaud & Raymond (1992). These small changes in the ionic equilibrium estimates are sufficient to explain the small discrepancy between the coronal holes in this work compared to older results. In all cases, coronal holes are found to be rather isothermal (other than a slight increase in T_e up to 1.4 $R_\odot$) and consistent in the inferred T_e values regardless of the inference method or period of the solar cycle, so it seems reasonable that improved ionic calculations are the only variable in this case.

As for the streamers, we find considerable complexity in the structure of the T_e. Unlike the coronal holes, it is difficult to give a singular value of the average streamer temperature, as it varies significantly at high spatial resolution. Overall, the T_e values in streamers range from about 1.4 to 1.65 MK, and we describe some of the fine-scale features in Section 4.1. These T_e

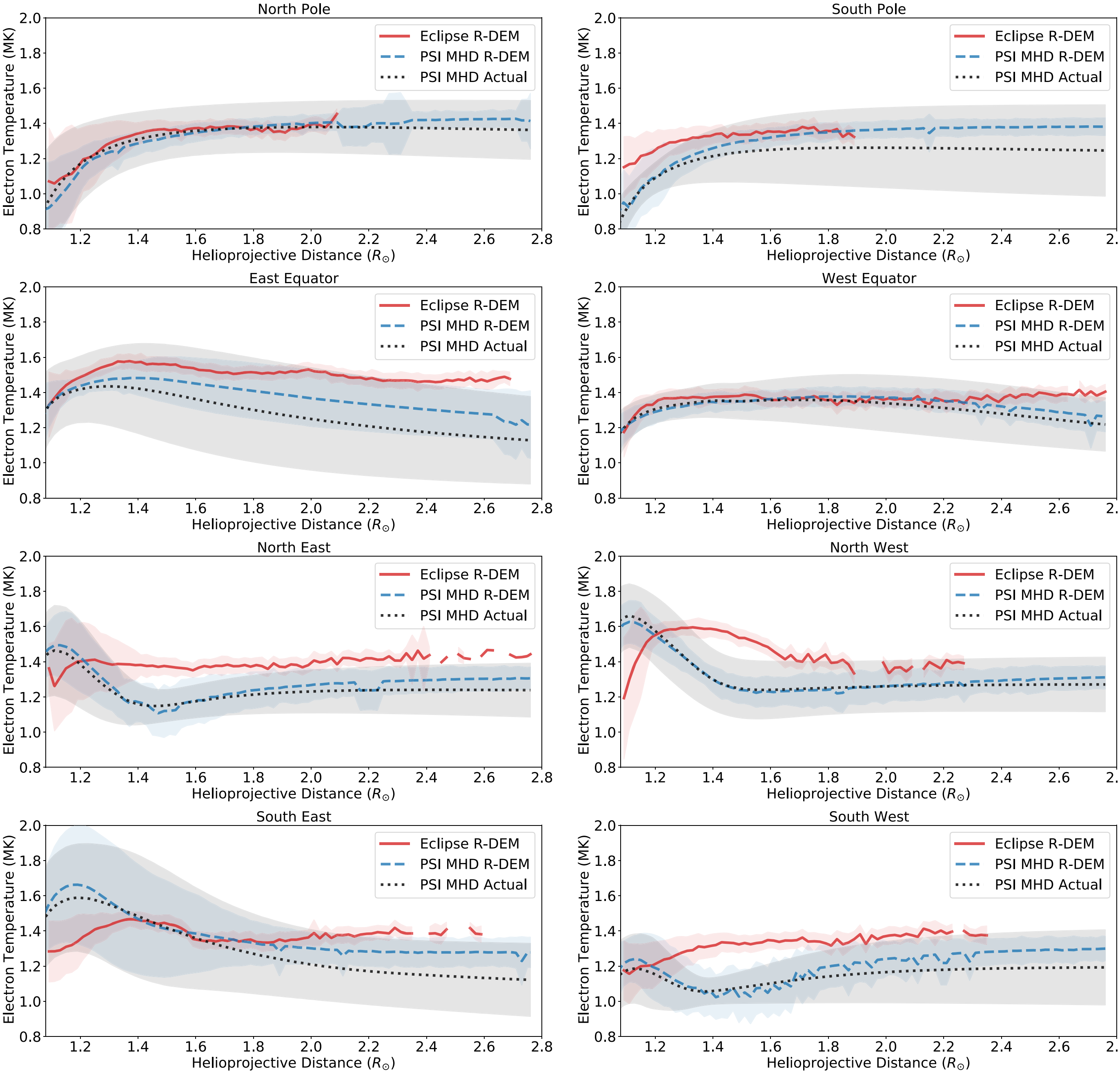

Figure 6. Radial traces of the R-DEMs from the eclipse data (solid red line), inferred from the MHD model (dashed blue line), and the actual MHD model (dotted black line). The traces are taken from the median average inside a 15° wedge centered on the cardinal direction indicated in the title of each panel. The filled bands show the 1σ standard deviation of the R-DEM distributions within the wedge.

values are relatively consistent with streamer observations from Raymond et al. (1997), who used UVCS observations (mostly of collisional lines) to find a rough temperature of about 1.6 MK. However, they did not perform a full T_e inversion. Indeed, Raymond et al. (1997) used lines from several different elements, so the observed brightness is convolved with the elemental abundance, which will vary due to the first ionization potential (FIP) effect (see Laming 2015). In this work, we used three lines of Fe, which removes any FIP effect dependence on the T_e inference. Similarly, Ko et al. (2002) found T_e values near 1.5 MK in "quiet-Sun" streamers and higher-T_e plasma above active regions (3 MK), but there were no active regions on the Sun during this particular eclipse. Additionally, Ulysses ionic composition data yielded 1.3–1.8 MK near the solar equator at solar minimum (Smith et al. 2003), which can be assumed to have originated from coronal streamers similar to the ones seen in this eclipse.

The contrast between the east and west streamers is a great example of the importance of these observations, specifically in showcasing the diversity of streamer dynamics even near solar minimum when no active regions are present on the Sun. There are turbulent structures inside the eastern streamer visible in the white-light image (top panel of Figure 1; see Habbal et al. 2021), which correspond to the highest T_e values anywhere in the corona during this eclipse. The western streamer, on the other hand, has a core with a much lower T_e that is almost

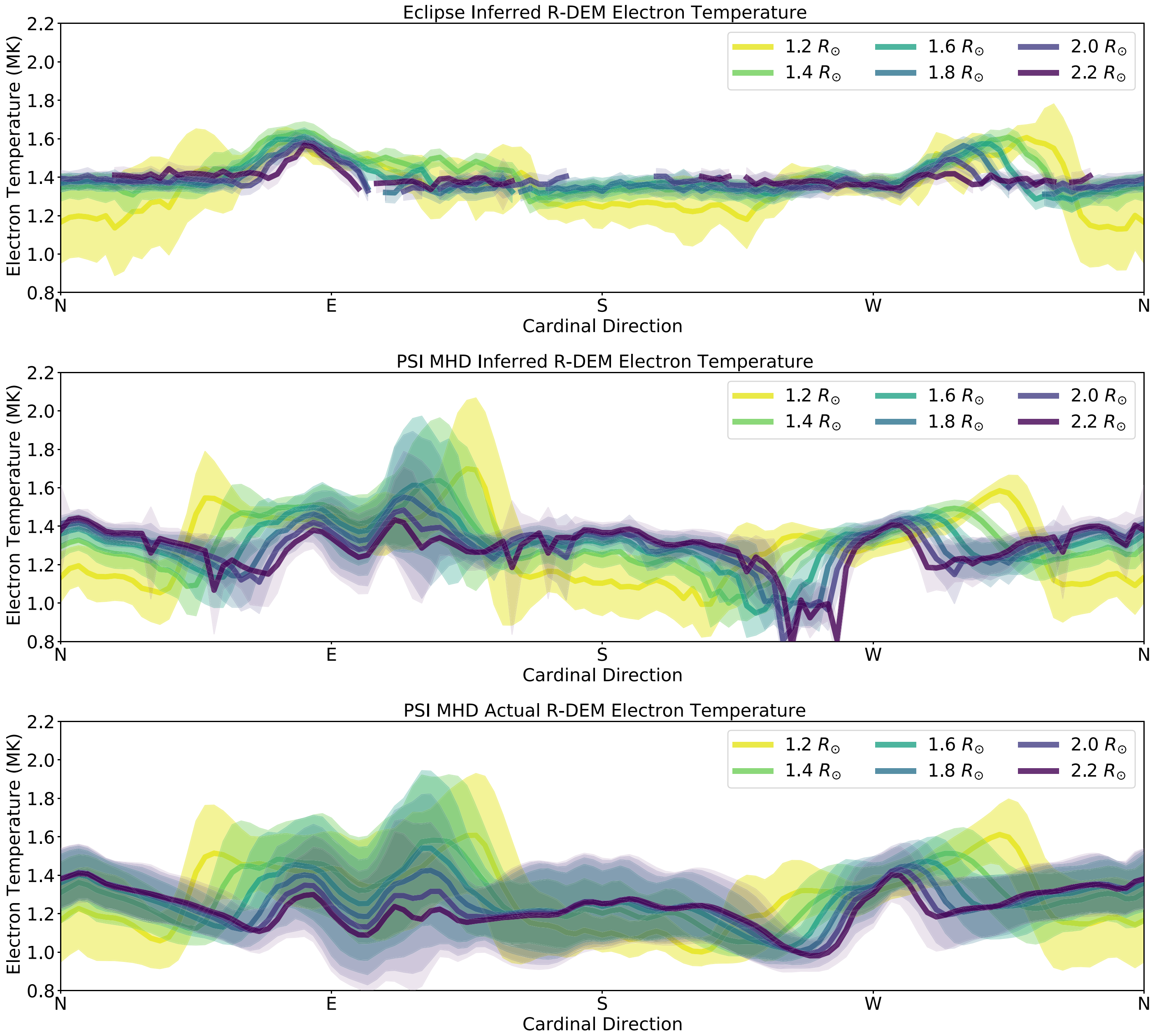

Figure 7. Latitudinal traces of the R-DEM median (solid lines) and standard deviation (shaded bands) at a selection of distances from the eclipse data (top panel), inferred from the MHD model (middle panel), and the actual R-DEM in the MHD model (bottom panel). The traces are taken as the median average R-DEM at a set of fixed helioprojective distances within a band of 0.1 $R_\odot$ of each distance (i.e., ±0.05 $R_\odot$).

indistinguishable from the coronal holes despite having a significantly higher density. These very different streamer temperatures indicate that there are never truly “quiet-Sun” streamers but rather different levels of activity and dynamics that can create quite unique structures. Chitta et al. (2023) recently found similar fine-scale structures, complexity, and diversity of coronal streamers using white-light and EUV observations along with MHD modeling—albeit without any T_e measurement.

Both the coronal holes and streamers have a slight rise in T_e from the base of the corona out to about 1.4 $R_\odot$. The cause of this ubiquitous T_e rise is not entirely clear, but there are two likely effects that could be contributing to the observed effect. One explanation might be a temperature-dependent scale-height effect. Aschwanden & Nitta (2000) described how, for an unresolved combination of hydrostatic loops, the higher-temperature loops will have larger scale heights. Thus, higher-temperature structures will have a shallower density gradient and will increasingly dominate the emission at larger distances. The same principle should apply to hydrodynamic flows with different base temperatures as well. The other possibility is that the temperature rise may actually be a change in the T_e of the plasma as it flows outward. Simulations of coronal heating often show a rise in temperature regardless of the exact heating mechanism used (e.g., Habbal et al. 1995; Verdini et al. 2010; Matsumoto & Suzuki 2014). Additionally, as with all optically thin plasmas, there are LOS effects from overlapping structures that may change the inferred temperature depending on the exact structures present in the corona. Disentangling these effects is not a trivial endeavor and is beyond the scope of this work. Nevertheless, these observations provide constraints for benchmarking future coronal heating simulations.

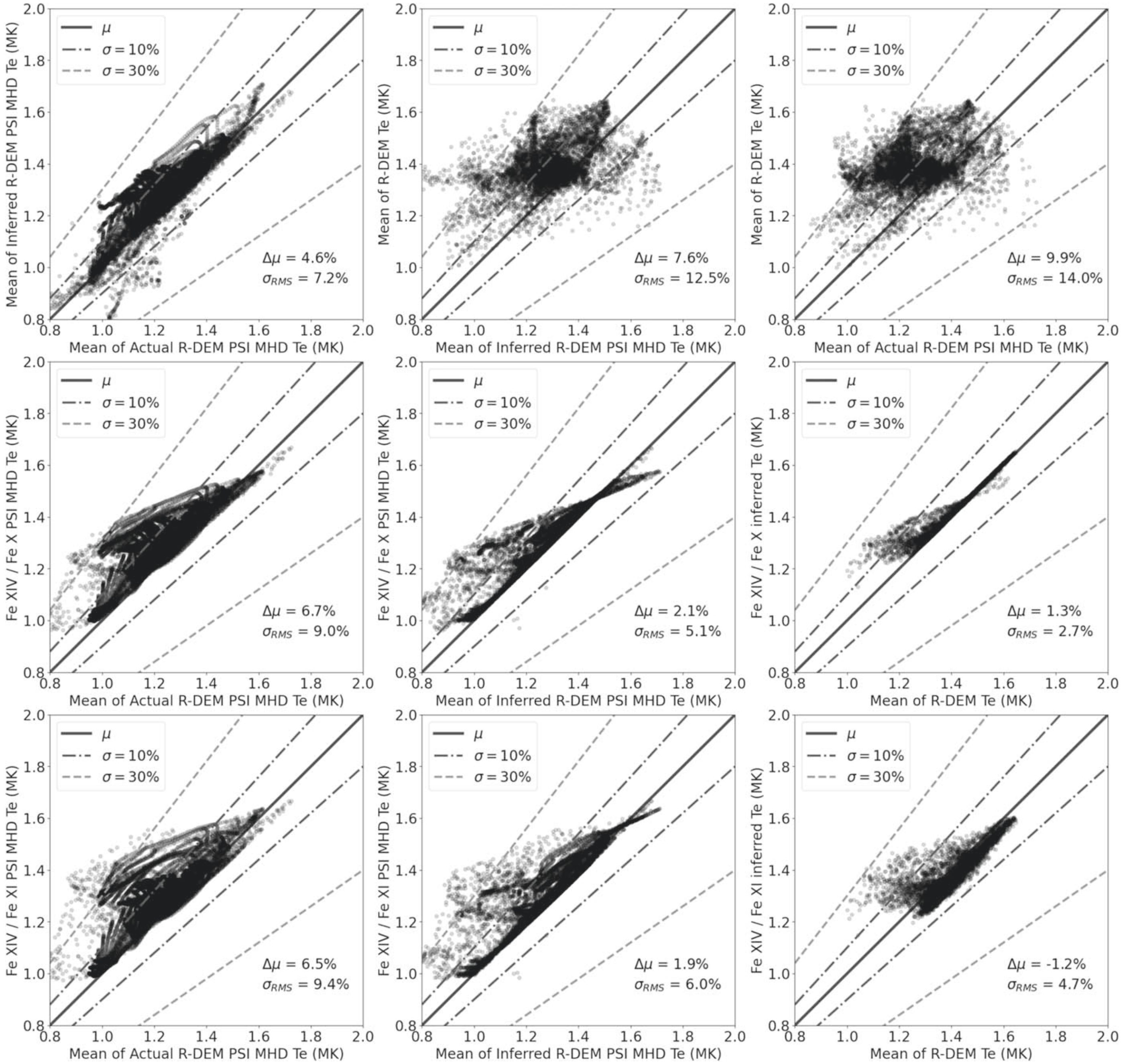

Figure 8. Scatter plot comparisons between the various R-DEM and two-line T_e results from the eclipse, the PSI MHD forward-modeled lines and the actual LOS average of T_e in the model.

5.2. On the Isothermality of the Middle Corona

One notable attribute of the eclipse R-DEM inversion results is that there is a large temperature spread (±0.2–0.35 MK) in the lower corona (i.e., the yellow lines at 1.2 $R_\odot$ in Figures 3, 4, and 7), with both much higher and lower T_e values than found with the two-line ratios (see Figure 1). This spread then disappears at higher distances. In fact, all of the eclipse R-DEMs converge to an almost isothermal T_e value (spread of <0.05 MK) by ≈ 1.4 $R_\odot$, which is highlighted by the low T_e standard deviation of the R-DEM (bottom-left panel of Figure 5).

The R-DEM inversion from the model has a somewhat wider T_e standard deviation throughout compared to the eclipse inversion, with the most dramatic spread occurring on the southern edge of the eastern streamer (see Figures 5 and 7). As discussed in Section 4.2.1, this three-line R-DEM inversion is not sensitive to distributions with widths less than about 0.2 MK but it is capable of detecting wider distributions. It is likely that if the actual distribution was significantly wider, then the R-DEM inversion should have detected it given its performance on the forward-modeled data. Our findings thus imply that in most of the corona, the emission-weighted temperature is near isothermal (to at least ±0.2) beyond 1.4 $R_\odot$, albeit with T_e differences between coronal holes and streamers on the POS. However, it is possible that an unknown systematic error related to photometric noise or other optical issues may be suppressing the inferred R-DEM width, especially since we do not have a high T_e precision with only three emission lines. Nevertheless, the isothermal nature of the corona appears at quite a low helioprojective distance where the line-emission signals were strong, and the MHD inversion results were able to recover wide R-DEMs in the eastern streamer out to 2.8 $R_\odot$.

The eclipse R-DEM inversion is indicating that (at the time of this eclipse) the corona below about 1.4 $R_\odot$ was a mixture of various structures along the LOS, which have a wide range of temperatures (i.e., streamers and coronal hole plumes overlapping on the POS), which is expected near the Sun given the wide range of T_e found in DEMs that have been achieved with EUV and X-ray observations (e.g., Pottasch 1964; Morgan & Taroyan 2017). There could also be scale-height effects contributing to this inference, as discussed in Section 5.1.

Beyond 1.4 $R_\odot$, the outer corona becomes an almost isothermal plasma at the root of the solar wind. This finding supports the recent work of Habbal et al. (2010, 2021), who found similar behavior in the corona and solar wind regardless of the phase of the solar cycle. We do find some small T_e standard deviation between the coronal structures but that spread is entirely on the plane of sky (POS) rather than along each LOS, and the majority of the corona becomes increasingly dominated by the highly isothermal coronal holes as the corona transitions into the solar wind.

Similar findings were reported by Del Zanna et al. (2023), who performed a collection of DEM and two-line ratio T_e inferences from data taken during this same eclipse. In particular, they found a rather isothermal T_e in the western streamer at 1.08 $R_\odot$ and a wider DEM at the same distance in the eastern streamer. The Del Zanna et al. (2023) analysis incorporated infrared spectra from AIR-Spec (Samra et al. 2022a, 2022b), an airborne spectrometer flown during the eclipse, finding rather consistent two-line T_e values for a number of infrared and EUV lines, supporting the concept that the corona was largely isothermal. However, that study was limited in its spatial coverage and elongation compared to the results presented here. Future work should incorporate additional lines as well as data from different phases of the solar cycle to better explore the behavior of the coronal R-DEM.

5.3. Testing the PSI MHD Simulation

Since the mean of the R-DEM inversion with the forward-modeled MHD lines is a close fit to the mean of actual temperature distribution in the model (see Section 4.2.1), we can reliably use the R-DEM results from the eclipse data to benchmark the PSI MHD simulation itself. The top middle and right panels of Figure 8 show direct comparisons between the eclipse-inferred R-DEM average T_e with the model R-DEM inversion (top middle) and the actual T_e mean in the model (top right). Both comparisons are remarkably similar, with the eclipse-inferred mean being somewhat higher than the model mean for the majority of LOSs. Specifically, the eclipse inversion is 7.6% ± 12.5% higher than the model inversion and 9.9% ± 14.0% higher than the actual model mean T_e. These comparisons indicate that the model is very close to reproducing the correct temperature distribution, with perhaps a slight underestimation of T_e on average. The model-inferred R-DEM also has slightly more temperature variability throughout the corona than the eclipse data, which is essentially isothermal at each distance (see Figure 7). The variability is especially notable in the coronal holes, where the model has a significant peak at the north pole (about 1.4 MK) compared to the minima in the northeast (1.1 MK) and southwest (1 MK). These small differences between the model and eclipse data are consistent with Paper II, which found that the Fe XI and Fe XIV lines were brighter in the coronal holes than the model predicted as well. Those differences were interpreted as an underheating of the polar magnetic field lines in the wave-turbulence-driven (WTD) heating model or possibly some other limitations in the MHD modeling approach.

The streamer core temperatures in the model inversion are generally close to the values in the eclipse data; however, the width and location of the streamer stalks are somewhat different. The eastern streamer in particular has a much larger latitudinal extent in the model and has two distinct peaks of T_e whereas the eclipse data only has one prominent peak with a few smaller stalks on the southern side. The model inversion also predicts that the eastern streamer T_e should decrease considerably with distance from the Sun, whereas the eclipse inversion maintains a relatively similar temperature out to at least 2.2 $R_\odot$. Both the model and the data show the width of the eastern streamer decreasing considerably at larger distances.

The MHD model makes even better predictions about the behavior of the western streamer, both in terms of the overall T_e values and a drift of the center of the streamer stalk from the northwest toward the south from 1.2 out to 2.2 $R_\odot$. Similar to the eastern streamer, the model does somewhat overestimate the width of the western streamer. Even though the trends in the western streamer are similar between the model and data, the model has the precise latitudinal location of the streamer somewhat farther south than in the eclipse data. This small difference in latitude may be explained by slight inaccuracies in the magnetic boundary conditions of the model, which incorporate synoptic magnetic measurements from the Sun–Earth line and estimates of the polar magnetic flux, both of which are imperfect proxies for the full-Sun–surface-flux distribution at a given instant of time (e.g., Riley et al. 2019).

5.4. Comparison to Two-line Inferences

The R-DEM mean T_e maps are rather similar to both the Fe XIV/Fe X and Fe XIV/Fe XI two-line ratio inferences of the T_e (bottom-right panels of Figure 1) for both the eclipse data and the MHD model. A collection of direct comparisons between both the model and eclipse two-line ratio inferences to their respective R-DEM means are shown in Figure 8. The two-line ratio inferences from the forward-modeled lines match the MHD average temperature quite well, with Fe XIV/Fe X (Fe XIV/Fe XI) returning a T_e value that is 6.7% ± 9.0% (6.5% ± 9.4%) higher than the actual LOS average (bottom-left panels). Similarly, the Fe XIV/Fe X (Fe XIV/Fe XI) ratio inference finds an average value that is 2.1% ± 5.1% (1.9% ± 6.0%) higher than the full R-DEM inversion of the MHD model (bottom-middle panels). In all cases, the average values are within the scatter of the collection of all LOS in the data set. As for the eclipse observations, the Fe XIV/Fe X T_e average is 1.3% ± 2.7% higher than the mean R-DEM inversion values (middle-right panel), whereas the Fe XIV/Fe XI T_e average is 1.2% ± 4.7% lower than the R-DEM mean (bottom-right panel).

Based on these comparisons, it is clear that the R-DEM inversion is able to better reproduce the actual LOS average temperature than the two-line ratios, but the simple two-line ratios are accurate to better than 10%. So, older eclipse data

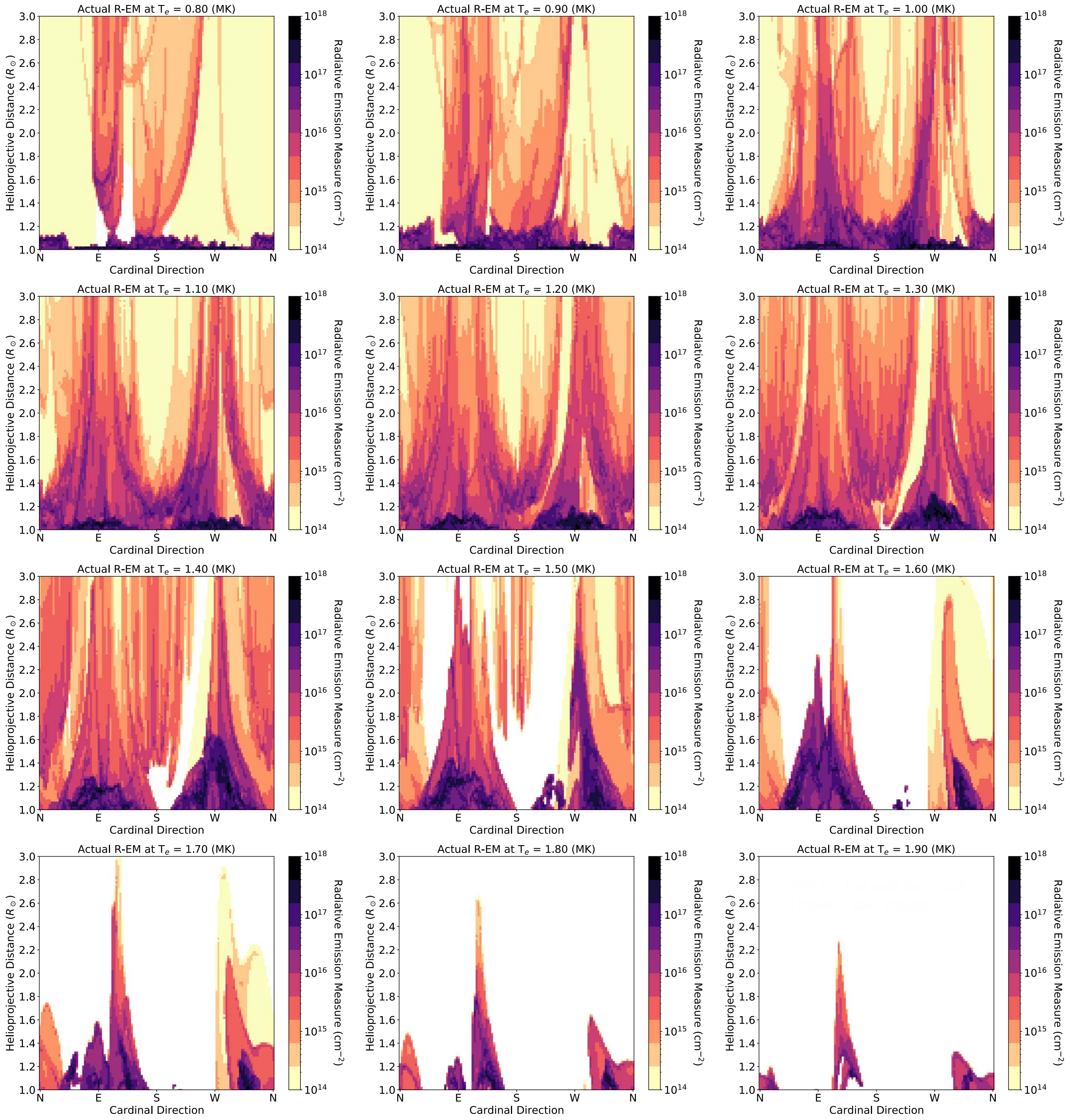

Figure 9. Selection of radiative emission measures from the PSI MHD model ranging from 0.8 to 1.9 MK. Each panel shows the integrated R-EM over a range of 0.01 MK. An animation with every 0.01 MK slice of the R-EM from 0.6 to 2.6 MK is available.

(An animation of this figure is available.)

with only two lines can still be reliably used to infer the average LOS T_e (e.g., Boe et al. 2020a). Still, there are tails of points at lower T_e in the two-line comparisons that diverge from the R-DEMs (i.e., the left side of the distributions in the middle and bottom panels of Figure 8), which correspond to the low regions of the corona that had a high standard deviation of the R-DEM T_e distribution. These low helioprojective regions are very likely a mix of colder open-field regions and hotter closed-field regions overlapping on the LOS, as illustrated by the R-EM of the PSI MHD model (see Figure 9 in the Appendix). These more complicated regions are not well resolved by a simple two-line average. Fortunately, this effect is rather confined to the lower corona (below 1.3 $R_\odot$). These lower regions of the corona are also where there is a considerable amount of collisional excitation in these lines. We isolated the radiative component of the observed brightness based on the collisional excitation fraction predicted by the MHD model (see Section 4.1; Paper II), but there could be uncertainties or systematic errors induced by this procedure. Future work should include observations of collisionally excited lines, such as the Fe XIII 1079.8 nm line (in addition to the radiative Fe XIII 1074.7 nm line), which could be used to observationally isolate the collisional excitation component without the need for the MHD model to perform the R-DEM inversion.

6. Conclusions

We have introduced the analog of a DEM for radiatively excited visible emission lines in the corona, which we call an R-DEM. The R-DEM methodology required a slight modification from traditional DEMs made with collisionally excited lines in the EUV and X-rays (see Section 1), which we detailed in Section 3.

We then applied the new R-DEM method to data from the 2019 total solar eclipse observations of Fe X, Fe XI, and Fe XIV (see Section 2) as well as to the same forward-modeled lines from the PSI MHD model for this eclipse (see Section 4.2). We then compared the actual LOS distribution of T_e in the model to the inferred R-DEM, finding that the R-DEM method with only three emission lines was able to accurately reproduce the average T_e values in the model (see Section 4.2.1). Moreover, the R-DEM method was able to recover the width of the distribution in regions of the PSI MHD model that had an LOS T_e standard deviation greater than about 0.2 MK but was unable to distinguish the T_e distribution over finer scales (see Section 5.2). Likely, this effect is caused by the broad T_e responses of these lines and the limit of only three used in the inversion. Future studies should incorporate additional lines to improve the temperature resolution of the R-DEM.

Given the demonstrated ability of this three-line R-DEM inversion to recover wide T_e distributions, it is interesting that the eclipse R-DEM results indicate that most of the corona has a very small standard deviation of the LOS T_e. In the low corona, below about 1.3 $R_\odot$, there are wide distributions in the T_e values, but beyond that distance, the corona seems effectively isothermal. The coronal hole plasma is remarkably isothermal at about 1.1–1.4 MK, while the quiescent streamers at the equator are closer to 1.4–1.65 MK. There is clearly a variation in the temperature between the quiescent streamers and the coronal holes, but the LOS variation of each structure is negligible.

This finding of near-isothermality supports the work of Habbal et al. (2010, 2021), who found that both the coronal and solar wind plasmas are strongly weighted to the charge state of Fe XI, which corresponds to about 1.3 MK. These results are also broadly consistent with Del Zanna et al. (2023), who performed DEM and two-line T_e inferences during the same eclipse with EUV and airborne infrared observations (Samra et al. 2022a). These consistent findings provide strong constraints for models of the solar wind—specifically, that relatively isothermal temperatures can be used for solar wind model initialization outside of the lower corona (above ≈1.4 $R_\odot$). Combining solar wind models and in situ ionic composition data with this R-DEM inversion method, applied to observations of visible and infrared coronal emission lines, could have immense potential for advancing our understanding of coronal heating and the exact nature of the link between the corona and solar wind.

The configuration of the corona during the 2019 eclipse, in particular, is an example of a near-perfect solar minimum corona. Future work could use this R-DEM method to test if there is a larger LOS T_e standard deviation during periods closer to solar maximum or if the corona remains essentially isothermal. R-DEM inversions would also be highly valuable when the corona has been disturbed by a coronal mass ejection. For example, Boe et al. (2020a) found changes in the LOS average T_e due to a passing CME during the 2017 eclipse with only a two-line T_e inversion but were unable to probe the LOS behavior with only two emission lines. Similar observations with three or more lines could be used to probe the complete temperature structure of an erupting CME in the middle corona (between 1.5 and 6 $R_\odot$).

The comparison between the R-DEM inversions of the eclipse and PSI MHD model also enabled a test of the model predictions. Similar tests had already been performed by Boe et al. (2021, 2022) for this specific simulation using the inferred K corona and two-line T_e inferences, respectively. In those papers as well as in this work (i.e., Section 5.3), the PSI MHD simulation is found to be an excellent match to the eclipse data. There is perhaps a very slight underestimation of the average T_e values by the model, but the differences are typically less than 10%. Still, these slight differences might point toward additional areas of improvement for coronal heating formulation in the MHD model. Further, the small discrepancies between the MHD model and eclipse data highlight the complexity of fine-scale structures in the corona that the model is not yet able to perfectly match. Regardless, the accuracy of the MHD simulation predictions is excellent.

The two-line ratio T_e inferences (from Boe et al. 2022) were then compared to the R-DEM inversions of both the eclipse and MHD model (see Section 5.4). In all cases, the inferred T_e from both the Fe XIV/Fe X and Fe XIV/Fe XI ratios are able to rather accurately infer the correct average R-DEM T_e, except for lower regions of the corona (below 1.3 $R_\odot$) where there is wider temperature distribution including a mixture of both colder (<1 MK) and hotter (>1.5 MK) plasmas along the LOS. Thus, observations with only Fe XIV and either Fe X or Fe XI can still be reliably used to infer the average LOS temperature.

As demonstrated in this work, visible and infrared emission lines are powerful tools for inferring the physical state of the corona out to at least 2.8 $R_\odot$. In Boe et al. (2022), the Fe XI line was observed as far as 3.4 $R_\odot$, a distance limited by the size of the detector rather than by a loss of signal. At future eclipses, instruments should be optimized to observe these emission lines to significantly larger helioprojective distances, which would be incredibly valuable for studying the formation and evolution of the solar wind in the corona, especially since these ions should freeze-in well below 5 $R_\odot$ (Boe et al. 2018; Gilly & Cranmer 2020). It may be possible to measure visible line emission out to 10 $R_\odot$ during eclipses, which could be directly compared to spacecraft plasma measurements from future perihelia of the Parker Solar Probe (Fox et al. 2016). Indeed, Antonucci et al. (2023) recently demonstrated with Metis on Solar Orbiter that the UV H I Lyα emission can be detected beyond 6 $R_\odot$. The eclipse-based observations thus continue to provide a key tool for studying the plasma properties of the corona and nascent solar wind.

The R-DEM method introduced here could be applied beyond eclipse observations as well. The new data from the ground-based UCoMP coronagraph (Tomczyk et al. 2021) in particular would be well suited for an application of this R-DEM method. UCoMP can observe the same, and several additional, visible and near-infrared lines. With a wide selection of emission lines, the R-DEM method should be able to infer the T_e distribution below ≈1.5 $R_\odot$. Additionally, the R-DEM method may be applied to the high-spatial-resolution coronal observations by DKIST (Rimmele et al. 2020). Studies with DKIST and UCoMP in the lower corona could be used to explore the effect of collisional excitation on the R-DEM inversion method (see Section 4.1), especially since both will observe the collisionally sensitive Fe XIII doublet (see Section 5.4). While DKIST is not as well suited for studying the formation of the solar wind compared to the eclipse observations, it could infer the R-DEM at exceptionally high spatial resolution in prominence cavities, polar plumes, jets, CMEs, etc., which could be of high value to multiple areas of solar physics.

Finally, recent demonstrations of the radiative self-excitation of the 17.1 and 19.3 nm EUV lines beyond 2 $R_\odot$ (Seaton et al. 2021) suggest that future work could even apply this R-DEM technique to EUV lines farther out in the corona—albeit after accounting for the complicated resonant scattering process driven by the collisional excitation of the same line lower down in the corona. Comparisons between similar inversions using lines all across the electromagnetic spectrum would be valuable for constraining the temperature distribution of coronal plasmas at a wide range of heliocentric distances and even could be applied to collisionless astrophysical plasmas generally.

Acknowledgments

Observables presented in this paper and other eclipse data from our group can be found at https://www.ifa.hawaii.edu/SolarEclipseData/. The PSI MHD model eclipse predictions can be found here: https://www.predsci.com/corona/.

Financial support was provided to B.B. by the National Science Foundation under award No. 2028173. S.H. and the 2019 eclipse expedition were supported under NASA grant No. NNX17AH69G and NSF grant No. AST-1733542 to the Institute for Astronomy of the University of Hawaii. C.D. was supported by the NASA Heliophysics Supporting Research and Living With a Star programs (grant Nos. 80NSSC18K1129 and 80NSSC20K0192).

Appendix
Actual R-DEM of the PSI MHD Model

The PSI/MAS MHD model is resolved at exceptionally high spatial resolution compared to previous global models (see Mikić et al. 2018) and generally at a higher spatial resolution than the eclipse data presented in this work. Specifically, the latitude and longitudinal mesh spacing is 0.009 rad (≈0°.5) except within 20° of the poles, where the mesh spacing is 0.0105 rad (≈0°.6). The radial mesh spacing is highly variable depending on the distance from the Sun, where the mesh spacing is less than 0.01 $R_\odot$ below 1.6 $R_\odot$, ≈0.025 $R_\odot$ at 2 $R_\odot$, and ≈0.05 $R_\odot$ at 3 $R_\odot$. Consequently, the spatial resolution of the model is considerably finer than the eclipse data in most of the corona, which has mesh points of 0.02 $R_\odot$ by 3° (in position angle). Further, each LOS integration through the model combines a multitude of bins so even when the model voxels are larger than the data resolution, their intersection probes the corona at a finer resolution.

For the purposes of comparing with the R-DEM inversions in this work, we integrated the actual R-DEM in the model with the same polar coordinate binning on the POS projection from Earth’s perspective and the same T_e bins used for the R-DEM inversion, which have a width of 0.01 MK (see Section 3.2). Since the actual R-DEM was integrated over these bins, the resulting integrals are R-EMs (i.e., Equation (5)). A collection of these R-EM maps are shown in Figure 9 for a selection of temperatures from 0.8 to 1.9 MK. An animation showing every R-EM from 0.6 to 2.6 MK is available. These R-EM maps show the amount of plasma at a given T_e along each LOS, in units of square centimeters (see Equation (5)). In this representation, the densities are not normalized for each LOS, as they were in Figures 3 and 4. In Section 4.2.1, we concluded that even though this binned T_e resolution is much higher than is possible to resolve using the three-line R-DEM used in this work, the R-EM maps are still interesting for revealing the finer details in the MHD simulation.

The model R-EMs show that there is a small density of plasma in the coronal holes at T_e values below about 1 MK, especially the southern coronal hole, and at the base of the corona below 1.2 $R_\odot$. Around 1 to 1.3 MK, the plasma density is somewhat uniformly distributed throughout the corona, roughly proportional to the bulk density. Above 1.5 MK, the plasma becomes increasingly confined to closed field lines in the streamers, and the extent of plasma at higher helioprojective distances decreases. The highest-T_e plasma (around 2 MK) in the southeastern streamer overlaps with regions that had very low T_e values as well.

In comparison with the eclipse data, we found that the average T_e in the model inversion is close to the eclipse data. However, the width of the model R-DEM inversion is considerably larger in some regions, particularly in the eastern streamer. It is not clear why the model has a wider distribution of temperature in certain regions than the eclipse data indicates but is likely related to the precise physical mechanism of the WTD approach to heating the corona in the model (Lionello et al. 2014; Downs et al. 2016; Mikić et al. 2018) and the inherent resolution of the global model grid, which naturally cannot resolve structures and contrasts below a certain size. To deduce the exact cause of these differences would require additional simulations where the precise assumptions and boundary conditions of the model are varied, which is beyond the scope of this work.

ORCID iDs

Benjamin Boe https://orcid.org/0000-0002-6396-8209
Cooper Downs https://orcid.org/0000-0003-1759-4354
Shadia Habbal https://orcid.org/0000-0003-4089-9316

References

Antonucci, E., Downs, C., Capuano, G. E., et al. 2023, PhPl, 30, 022905
Arnaud, M., & Raymond, J. 1992, ApJ, 398, 394
Aschwanden, M. J., Boerner, P., Caspi, A., et al. 2015, SoPh, 290, 2733
Aschwanden, M. J., & Nitta, N. 2000, ApJL, 535, L59
Boe, B., Habbal, S., Downs, C., & Druckmüller, M. 2021, ApJ, 912, 44
Boe, B., Habbal, S., Downs, C., & Druckmüller, M. 2022, ApJ, 935, 173
Boe, B., Habbal, S., Druckmüller, M., et al. 2018, ApJ, 859, 155
Boe, B., Habbal, S., Druckmüller, M., et al. 2020a, ApJ, 888, 100
Boe, B., Habbal, S., & Druckmüller, M. 2020b, ApJ, 895, 123
Boerner, P., Edwards, C., Lemen, J., et al. 2012, SoPh, 275, 41
Cheng, X., Zhang, J., Saar, S. H., & Ding, M. D. 2012, ApJ, 761, 62
Cheung, M. C. M., Boerner, P., Schrijver, C. J., et al. 2015, ApJ, 807, 143

Chitta, L. P., Seaton, D. B., Downs, C., DeForest, C. E., & Higginson, A. K. 2023, NatAs, 7, 133
Del Zanna, G., Dere, K. P., Young, P. R., & Landi, E. 2021, ApJ, 909, 38
Del Zanna, G., & Mason, H. E. 2018, LRSP, 15, 5
Del Zanna, G., Samra, J., Monaghan, A., et al. 2023, ApJS, 265, 11
Dere, K. P., Landi, E., Mason, H. E., Monsignori Fossi, B. C., & Young, P. R. 1997, A&AS, 125, 149
Downs, C., Lionello, R., Mikić, Z., Linker, J. A., & Velli, M. 2016, ApJ, 832, 180
Doyle, J. G., Teriaca, L., & Banerjee, D. 1999, A&A, 349, 956
Esser, R., Habbal, S. R., Coles, W. A., & Hollweg, J. V. 1997, JGR, 102, 7063
Fox, N. J., Velli, M. C., Bale, S. D., et al. 2016, SSRv, 204, 7
Gilly, C. R., & Cranmer, S. R. 2020, ApJ, 901, 150
Goryaev, F., Slemzin, V., Vainshtein, L., & Williams, D. R. 2014, ApJ, 781, 100
Güdel, M., Audard, M., Magee, H., et al. 2001, A&A, 365, L344
Guennou, C., Auchère, F., Soubrié, E., et al. 2012a, ApJS, 203, 25
Guennou, C., Auchère, F., Soubrié, E., et al. 2012b, ApJS, 203, 26
Habbal, S. R., Druckmüller, M., Alzate, N., et al. 2021, ApJL, 911, L4
Habbal, S. R., Esser, R., & Arndt, M. B. 1993, ApJ, 413, 435
Habbal, S. R., Esser, R., Guhathakurta, M., & Fisher, R. R. 1995, GeoRL, 22, 1465
Habbal, S. R., Morgan, H., Druckmüller, M., & Ding, A. 2010, ApJL, 711, L75
Hannah, I. G., & Kontar, E. P. 2012, A&A, 539, A146
Kashyap, V., & Drake, J. J. 1998, ApJ, 503, 450
Kepa, A., Sylwester, B., Siarkowski, M., & Sylwester, J. 2022, ApJ, 927, 19
Kepa, A., Sylwester, J., Sylwester, B., Siarkowski, M., & Stepanov, A. I. 2006, SoSyR, 40, 294
Ko, Y.-K., Fisk, L. A., Geiss, J., Gloeckler, G., & Guhathakurta, M. 1997, SoPh, 171, 345
Ko, Y. K., Fisk, L. A., Gloeckler, G., & Geiss, J. 1996, GeoRL, 23, 2785
Ko, Y.-K., Raymond, J. C., Li, J., et al. 2002, ApJ, 578, 979
Laming, J. M. 2015, LRSP, 12, 2
Landi, E., & Testa, P. 2014, ApJ, 787, 33
Lionello, R., Velli, M., Downs, C., et al. 2014, ApJ, 784, 120
Matsumoto, T., & Suzuki, T. K. 2014, MNRAS, 440, 971
Mikić, Z., Downs, C., Link, J. A., et al. 2018, NatAs, 2, 913
Morgan, H., & Pickering, J. 2019, SoPh, 294, 135
Morgan, H., & Taroyan, Y. 2017, SciA, 3, e1602056
Munro, R. H., & Jackson, B. V. 1977, ApJ, 213, 874
O'Dwyer, B., Del Zanna, G., Mason, H. E., Weber, M. A., & Tripathi, D. 2010, A&A, 521, A21
Pickering, J., & Morgan, H. 2019, SoPh, 294, 136
Plowman, J., Kankelborg, C., & Martens, P. 2013, ApJ, 771, 2
Pottasch, S. R. 1964, SSRv, 3, 816
Raymond, J. C., Kohl, J. L., Noci, G., et al. 1997, SoPh, 175, 645
Riley, P., Linker, J. A., Mikic, Z., et al. 2019, ApJ, 884, 18
Rimmele, T. R., Warner, M., Keil, S. L., et al. 2020, SoPh, 295, 172
Samra, J. E., Madsen, C. A., Cheimets, P., et al. 2022a, ApJ, 933, 82
Samra, J. E., Marquez, V., Cheimets, P., et al. 2022b, AJ, 164, 39
Seaton, D. B., Hughes, J. M., Tadikonda, S. K., et al. 2021, NatAs, 5, 1029
Smith, E. J., Marsden, R. G., Balogh, A., et al. 2003, Sci, 302, 1165
Tomczyk, S., Landi, E., Berkey, B., et al. 2021, AGUFM, 2021, 2089
Verdini, A., Velli, M., Matthaeus, W. H., Oughton, S., & Dmitruk, P. 2010, ApJL, 708, L116
Weber, M. A., Schmelz, J. T., DeLuca, E. E., & Roames, J. K. 2005, ApJL, 635, L101
Withbroe, G. L. 1978, ApJ, 225, 641